In-situ mapping of local orientation and strain in a fully operable infrared sensor

C. Yildirim, D. Brellier, Raphaël Pesci, F. Boulard, N. Baier, T. Zhou, T. Nguyen-Thanh, P. Gergaud, T. Schulli, P. Ballett

In-situ mapping of local orientation and strain in a fully operable infrared sensor

C. Yildirim[a,b,*], D. Brellier[a], R. Pesci[c], F. Boulard[a], N. Baier[a], T. Zhou[b], T. Nguyen-Thanh[a], P. Gergaud[a], T. Schulli[b], P. Ballet[a]

[a] *Université Grenoble Alpes CEA, Leti, 38000, Grenoble, France*
[b] *European Synchrotron Radiation Facility, 71 Avenue des Martyrs, CS40220, Grenoble Cedex 9 38043, France*
[c] *ENSAM-Arts et Métiers Sciences and Technologies, LEM3 UMR CNRS 7239, 4 Rue Augustin Fresnel, Metz Cedex 3, 57078, France*

A B S T R A C T

Hybridized focal plane array (FPA) HgCdTe (MCT) sensors are the workhorse of high performance infrared detectors covering a broad range of applications from space investigation to gas monitoring. Despite the improvements in the performance of these sensors in the last decades, device failure due to the lattice and thermal expansion mismatches between MCT and the Si readout circuit still affects the overall MCT detector performance. In this work, we use *in-situ* dark-field X-ray microscopy (DFXM) to map the structural variations of a fully operable MCT sensor at temperatures down to 80 K. We report, for the first time, on the nanoscale structural evolution over a large population of photodiodes at operating temperatures with high spatial and angular resolution. Our results show that lattice distortion and strain in the MCT epilayer increases at lower temperatures. The FWHM values of the rocking curves reach up to 0.02° at 80 K, three times higher than the room temperature value. The thermal cycle results show that the thermal effects are almost completely reversible and the measured strain is in the elastic regime. We discuss the origin of the temperature-generated structural modifications using complementary finite element modelling.

1. Introduction

HgCdTe (MCT) is today's material of choice for developing high performance infrared detectors. The tunable bandgap of MCT provides a wide spectrum of infrared (IR) detection from very short wavelengths (1.5-2 μm) to mid (3–5 μm) and long wavelengths (8–12 μm). Thus the applications of MCT covers a broad range including telecoms, gas monitoring, space investigation and astronomy. Continuous improvements in device performance have been achieved and demonstrated over the last decades thanks to material optimization and novel photodiode architectures [1,2]. Requirements for increased resolution recently led to the development of large focal plane arrays (FPAs) with $\geq$ 1 Megapixel having a pixel size of 15 μm or less. Nevertheless, device failure in the form of a few individual pixel deviations to nominal diode electro-optical characteristics still impacts overall MCT detector yield and industrialization [3].

Today, the physical origin of defective photodiodes is the core of intense research. The investigation of epitaxial mismatch strain between the MCT layer and CdZnTe (CZT) substrate [4] is of particular interest, as is the impact of the different processing steps throughout device fabrication such as etching, ion implantation, surface passivation, metallization and annealing [5,6]. Moreover, the thermal mismatch between MCT and Si readout circuit in 2D FPAs is another source of the defective photodiodes, since these sensors typically operate at 80 K [7–10]. While material issues at the wafer scale can be addressed through conventional techniques [11,12], technological processes resulting in pixel failures require more localized probes. We recently employed Laue micro-diffraction to determine localized strain fields in HgCdTe along the fabrication of individual diodes [5] yet with a rather narrow field of view (one or two pixels at most) and limited spatial resolution.

Here, we present an *in-situ* study of the structural variations in a fully operable MCT IR sensor using Dark Field X-ray microscopy (DFXM) at temperatures down to 80 K. Dark field X-ray microscopy (DFXM) is a non-destructive, diffraction-based imaging technique that allows mapping of strain and orientation in embedded crystals with high spatial and angular resolution reaching up to 30 nm and 0.001°, respectively [13–16]. High resolution coupled with the large field of view (hundreds of microns) makes DFXM an ideal tool to study defective photodiodes not only individually but also

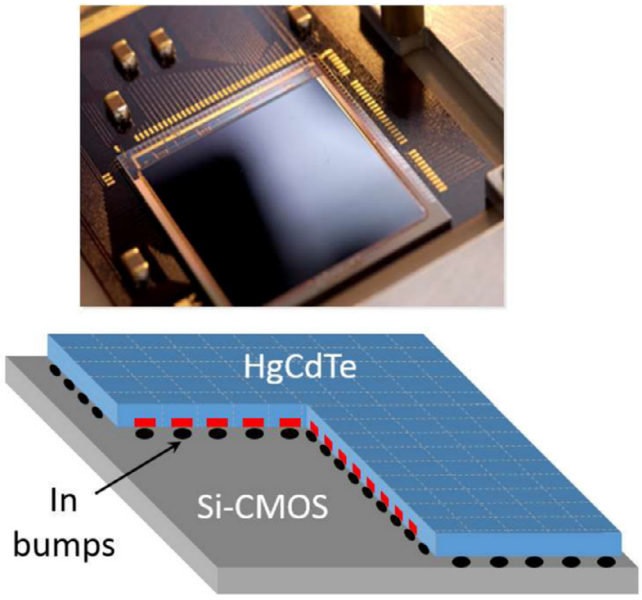

Fig. 1. Photo and the schematics of the device showing the different layers of the overall design.

statistically at operating temperatures. We report, for the first time to our knowledge, on the structural properties at the nanoscale over a large population of photodiodes within a fully operable IR detector device. Moreover, our results provide an unprecedented demonstration of DFXM at cryogenic temperatures.

2. Experimental methods

2.1. Device fabrication

Backside illuminated HgCdTe midwave IR 640x512 FPA was used in this study. HgCdTe was grown by liquid phase epitaxy on lattice matched CdZnTe (111) substrate. N on P photodiodes were formed by ion implantation with a 15 μm pixel pitch. Fig. 1 shows schematics of the device. On the upper side part of the device, one can see and array of photodiodes (640 x 512) with 15 μm pixel size manufactured on HgCdTe (MCT) active layer grown on a CdZnTe substrate. On the lower side, pixel biasing, readout and multiplexing performed by a silicon Read Out Integrated Circuit (ROIC) can be seen. These two parts of the device were coupled (i.e. hybridized) with indium bumps so that each photodiode of the MCT array is connected to a pixel of the silicon ROIC with a direct injection input stage [17]. More details on the process are given elsewhere [18]. Prior to DFXM the substrate was removed leading to a 6 μm thick HgCdTe layer.

2.2. Dark field X-ray microscopy

All DFXM experiments were carried out at the beamline ID01 of the European Synchrotron Radiation Facility (ESRF) [19]. X-rays with 8 keV energy were selected from an undulator source using a double-bounce monochromator positioned at 34 m from the source. The incident beam was focused on to an on-sample spot size of 270 μm (horizontal) × 240 μm (vertical) using a Be compound refractive lens (CRL) transfocator. An X-ray objective CRL comprising 55 parabolic Be lenslets was positioned at 95 mm downstream of the sample. An Andor CMOS camera with 2560 × 2160 pixels with 6.5 μm pixel size situated at about 6 m from the sample was used to collect the magnified dark field images. The resulting spatial resolution is about 120 nm/px. The sample was positioned such that the out of plane 333 Bragg reflection was selected in horizontal scattering geometry ($2\theta = 77.15^\circ$). The local orientation of the sample was measured by tilting the sample in 41 steps over a 0.2° range. For rocking curve analyses, the sample is tilted around the diffraction vector. The strain mapping was carried out in the form of $\theta - 2\theta$ radial scans over 0.4° in 41 steps. A cryostat was used to perform *in-situ* cooling down to 80 K.. Cryogenic conditions on the sample were achieved using a cryo-arm that held the sample under vacuum during the DFXM measurements. This cryogenic sample environment system was designed specifically for the beamline ID01 to meet the ambitious requirements of mechanical stability. It can operate between 2K and room temperature with typical ramp speeds of ≈ 10 K/min in cooling and heating modes.

2.3. Electro-optical characterization

The detector was characterized electro-optically before and after the DFXM experiments to validate the robustness of the results and to detect any possible X-ray beam damage to the functionality of the detector. In essence, the effect of radiation on these type of detectors provides potentially important information for space applications [20,21]. The electro-optical characterization comprises two parts. The first part involves the electrical characterization of the ROIC alone including reset voltage and its related RMS noise, whereas the second part consists of an electro-optical characterization of the whole detector including photodiode current, RMS noise, contrast, and sensitivity. Extracting the main characteristics of the photodiode array is possible by subtracting the electrical characteristics of the ROIC, which act as a reference point to the electro-optical measurements.

ROIC pixel is composed of several functional blocks: the input stage, the integration and reset node, and finally the multiplexer. Note that the MCT photodiode array of the detector analyzed here was split into 16 different variants during the manufacturing process (i.e. Fig. 2(a)). The varying parameters are linked to the geometry of the P-N junction.

3. Results

3.1. Electro-Optical characterization results

3.1.1. Array characterization pre DFXM experiment

We performed electro-optical measurements to fully characterize the detector prior to the DFXM experiment. The detector was integrated into a cryostat, cooled by liquid nitrogen down to 78 K. All the detector biases and logical chronograms to operate the detector were set to their nominal values. Notably, the diodes bias was 100 mV and the image frame rate of the detector was set to 19.4 Hz.

Amongst different measurements and results, four are presented and discussed here:

- the mapping of the reset voltage of the ROIC
- the mean photocurrent, I_{ph}, (on each variant of the array) as a function of photodiode voltage
- the responsivity of the array in A/K (difference in current measured under homogeneous blackbody illumination at 20 and 30 °C; measured with numerical aperture F/4)
- the excess noise of the photodiode array.

The last item is a calculation. ROIC RMS noise is quadratically subtracted from total RMS noise measured under a specific IR flux. The result is then divided by the theoretical RMS noise: σ_{th} calculated from the photocurrent under the same flux $\sigma_{th} = \sqrt{2qI_{ph}}$.

Table 1
Eletro-optical characterization results before and after the DFXM experiment.

Sample State	ROIC reset voltage	Responsivity Dispersion	Excess Mean Noise
Before DFXM	3 V ± 9 mV	1.3 - 4.1 %	1.026 ± 0.12
After DFXM	2.94 V ± 41.1 mV	1.5 - 3.8 %	0.976 ± 0.146

3.1.2. Array characterization post DFXM experiment

The same measurements were carried out after the DFXM experiment. Table 1 summarizes the overall electro-optical characterization results before and after the DFXM experiment. Although the mean reset voltage of ROIC was not dramatically affected, some areas present high voltage variations due to the X-ray beam exposure, resulting in a standard deviation of 41.1 mV (a factor of 4.6 compared to the first measurement). Nevertheless, the responsivity mapping (Fig. 2(a) and (b)) shows no dramatic impact. The dispersion for the non-exposed region ranges from 1.6% to 3.8% depending on the given variant whereas dispersion values between 1.5% to 3.1% are found for the exposed variants. Moreover, these values are very similar to measurements before the experiment (Table 1). There is no significant difference in dispersion values between exposed and the non-exposed variants. This indicates that the photodiodes did not suffer from a major damage during X-ray exposure.

However, a focus on a specific area (Fig. 2(c)) clearly shows a distinct pattern corresponding to the exposed area (Z2). To better understand this observation, an analysis of the current-voltage (I-V) characteristic is needed.

I-V characteristics of squares of 100 diodes in variants 4 (not exposed to X-rays) and 9 (exposed) were analyzed. These areas have the same technological variant implemented, thus they are well suited for comparison. In the V9, the diodes are chosen at the top left of the variant square at coordinates x, y (0.51, 1.6) mm, thus in a highly exposed zone.

The mean I-V characteristics are presented in (Fig. 2(d)). It is important to note that these values are calculated from the whole array, thus statistically dominated by healthy pixels. A shift of 60mV is remarkably low in comparison to the unexposed regions as seen in Fig. 2(d) (about 300mV). In V4, there is no significant difference between the measurement before and after the DFXM experiment. In contrast, the diodes in V9 were particularly impacted with a mean I-V highly shifted towards lower voltages. This behavior is the result of the shift of the reset voltage. Thus the selected photodiodes in V9 are biased at a different voltage than the other photodiodes. As a consequence their current is a few pA higher, but due to the low standard deviation on a given area (typically 1.25 pA in V9) these diodes appear to have a different behavior with an excess current and responsivity.

These measurements show that X-ray exposure has an impact on the functionality of the whole detector. Yet this impact is exclusively limited to the silicon ROIC, with a substantial degradation of one or some of the functional pixel blocks for the pixels in the exposed areas. The MCT layer seems to be particularly robust to the X-ray flux during this experiment. To conclude, the electro-optical characterizations validate the robustness of the MCT layer for further orientation and strain characterization using DFXM.

3.2. DFXM Results

3.2.1. Orientation maps and pixel by pixel analyses of Z1

Fig. 3(a) shows the DFXM experimental set up. The diffracted beam is magnified onto a CCD located at about 6 m from the sample using an X ray objective. The diffraction set up was in horizontal geometry. The field of view captured by the CCD was 495 μm × 260 μm.

Fig. 3(b) and (c) shows the optical micrograph and architecture of the studied zone, Z1. The DFXM images were collected ≈ 150 μm above the square shown in these images.

Fig. 3(d), (e), and (f) show the reconstructed center of mass orientation maps from the sample tilt (i.e. rocking curve) of Z1 at 300 K, 110 K, and 80 K respectively. These maps are generated by stacking DFXM images together and fitting a Gaussian to the individual rocking curves at each pixel of the CCD detector. All images were pre-processed using a rotational noise-reducing filter prior to the stacking. The reciprocal space information (θ and 2θ) of each pixel in the CCD detector was then found by this Gaussian fit. The center-of-mass plots (i.e. peak position) then represent the local orientation or strain around the centroid value of a given scan. A detailed explanation to the generation of these maps can be found elsewhere [22]. Exemplary rocking curves are provided in the Supp. Mat. The different implantation regions shown in Fig. 3(c) are clearly visible in the orientation map. The 15 μm-sized MCT pixels can be seen mostly on the high-θ side of the rocking curve. There are some pixels that are oriented with a difference of about 0.01° compared to the rest of the pixels to both sides of the rocking curve (the blue and yellow pixels). Looking at the region right next to the square MCT pixels, one can see round features that are of different mechanical contacts (shown by the yellow arrows in Fig. 3(d)). These regions have higher angular spread than the pixel counterparts.

Upon cooling down to 110 and 80 K, significant structural changes are observed. The images show not only an overall increase in the angular spread, but also local deterioration of the pixels and regions with round mechanical contacts (zones marked by the yellow arrows in Fig. 3(d)). At first glance, the pixels in the map taken at 100 K no longer have their square shapes. Moreover, their orientation is vastly different compared to the ambient conditions. For instance, the saturated blue and yellow colors indicate that the angular spread of the MCT pixels has reached more than 0.07° between one pixel and its neighbour. While the alternating high and low θ orientation variations (blue and yellow) are observed horizontally, one can observe vertical lines of the same orientation across the images in Fig. 3(e), (f). Similar to the deterioration of the 15 μm-sized pixels, the round features (shown with yellow arrows in Fig. 3(d)) located at the left hand side of the pixels show a completely different picture at lower temperatures than at ambient temperature. The round features have almost vanished, and lower θ (blue color) lines link the borders of this region. These structural changes are further emphasized on cooling down to 80 K. The full view of Z1 shows increased lattice distortions across the field of view at lower temperatures. In order to see the structural variations of the individual pixels, we conducted a pixel by pixel analysis on the region Z1 of the sample. Fig. 4 shows the results of this analysis. Fig. 4(a) and (c) shows the rocking curve center of mass maps at 300 K and 80 K. The red symbols in these images mark the points where we extracted the angular position of a given pixel from its center. Fig. 4(b) shows the distribution of the peak position of these points as a function of their pixel number starting from the top left. Similarly, in Fig. 3(d) at 300 K, the pixels show a positive θ value around the nominal θ value. The normalized peak positions of these points are less than 0.01° from nominal(i.e. the red bars shown in the Fig. 4(b)). However, upon cooling down to 80 K, the lattice distortion increases and gives rise to high fluctuations of the peak position. These fluctuations are present to-

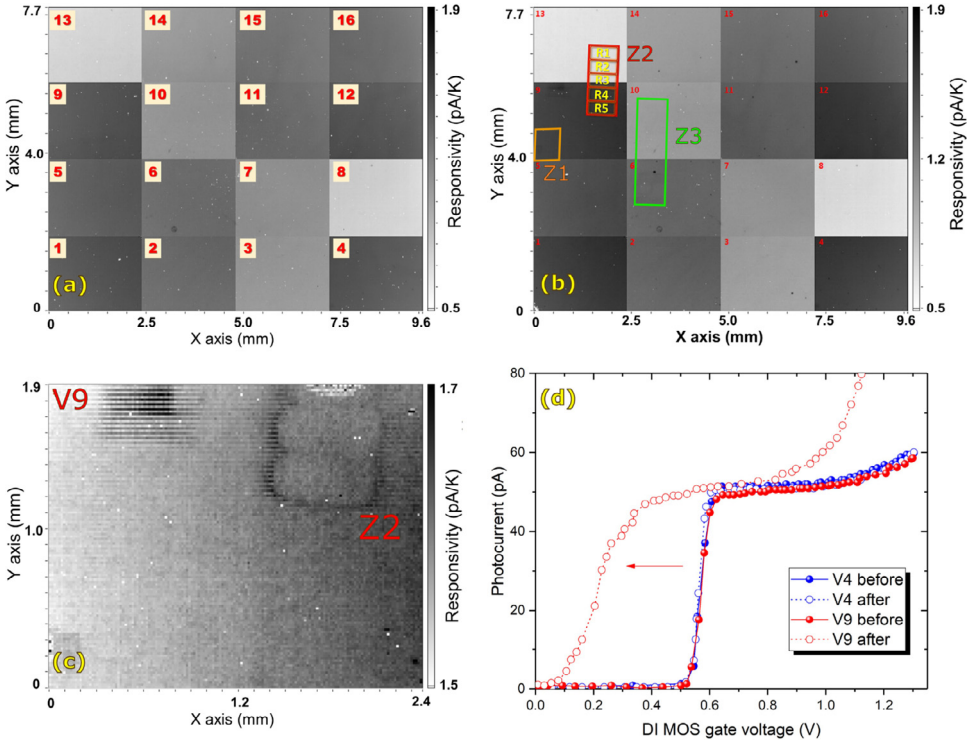

Fig. 2. Electro-optical characterization of the detector before and after the DFXM experiment. Responsivity map of the IR sensor before (a) and after (b) the DFXM experiment showing the 16 process variants. The colored rectangles (Z1, Z2, and Z3) mark the regions of interest of the DFXM experiment. Z2 was divided into 5 separate regions as shown in (b) (i.e. R1 to R5) where R3 overlaps on two different variants, namely V9 and V13. Zoom of the responsivity map for variant 9 showing Z2 after X-ray exposure (c). $I-V$ characteristics of two groups of 100 pixels in the exposed (V9) and non-exposed (V4) variants before and after the DFXM experiments (d).

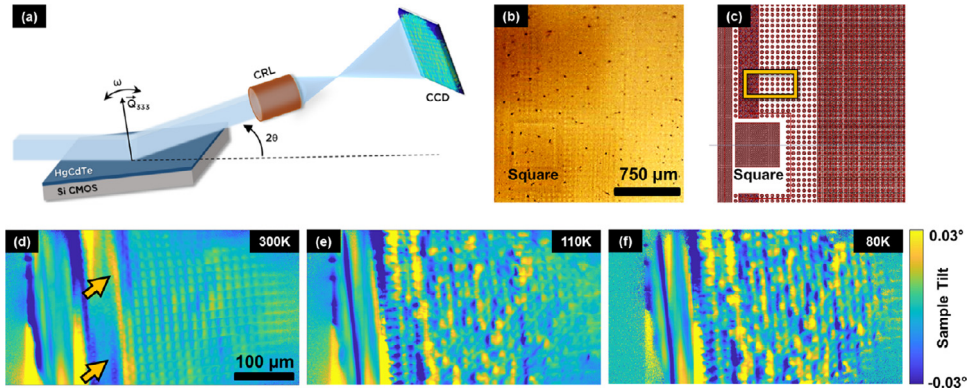

Fig. 3. (a) DFXM experimental set up. The sample is illuminated by transfocator-collimated X-ray beam. The 333 Bragg reflection is probed in reflection geometry. The angles ω and 2θ correspond to the tilt angles around the Q_{333} scattering vector of the MCT crystal. The X-ray objective CRL is placed along the diffracted beam to magnify the projection of the diffracting MCT crystal. The far field CCD detector is at about 6 m from the sample. (b) Optical microscope image of the investigated area, (c) the architecture of the same area in terms of implantation and contact. The yellow rectangle shows the regions studied with DFXM, z1. Reconstructed peak position maps of the sample orientation at (d) 300 K (e) 110 K and (f) 80 K. The yellow arrows in (d) show the round-shaped mechanical contacts, which are found at the left side of the yellow square in (c). The color scale is the same for all maps. (For interpretation of the references to colour in this figure legend, the reader is referred to the web version of this article.)

ward both sides of the rocking curve (i.e. high and low θ). This indicates that the distortions of the pixels have compressive and tensile components from one pixel to another. Fig. 4(d) illustrates the overall increase of the spread of the rocking curve at different temperatures, showing the increase of the FWHM of these pixels due to lattice distortions upon cooling.

3.2.2. Strain mapping on Z1 and Z2

Fig. 5(a-h) show the relative axial strain evolution of selected regions R1 and R5, in Z2 at different temperatures.The studied regions in Z2 correspond to two different variants of the IR detector. R1 and R2 are located in the variant number 13 whereas R4 and R5 are in variant 9 (i.e. Fig. 2(b)). R3 is situated accross the border between these two variants. The strain maps were constructed from the center of mass positions obtained by the θ-2θ radial strain scans. One can calculate the axial stress using Hooke's law (see the Supplementary document S1.) The measured strain is of the order of a few 10^{-4}.

In the area Z2, regardless of the region, most of the pixels of the sensor are under compressive stresses of $\approx$ 1–3 MPa acting on them and the stress distribution is rather homogeneous at room temperature. As the temperature is decreased, the overall stress spread increases at all the regions of Z2. At 150 K individual pixels start to have alternating stress states of tension and compression. This effect becomes more prominent upon further decrements of temperature. Looking at R1, some positively-strained zones that

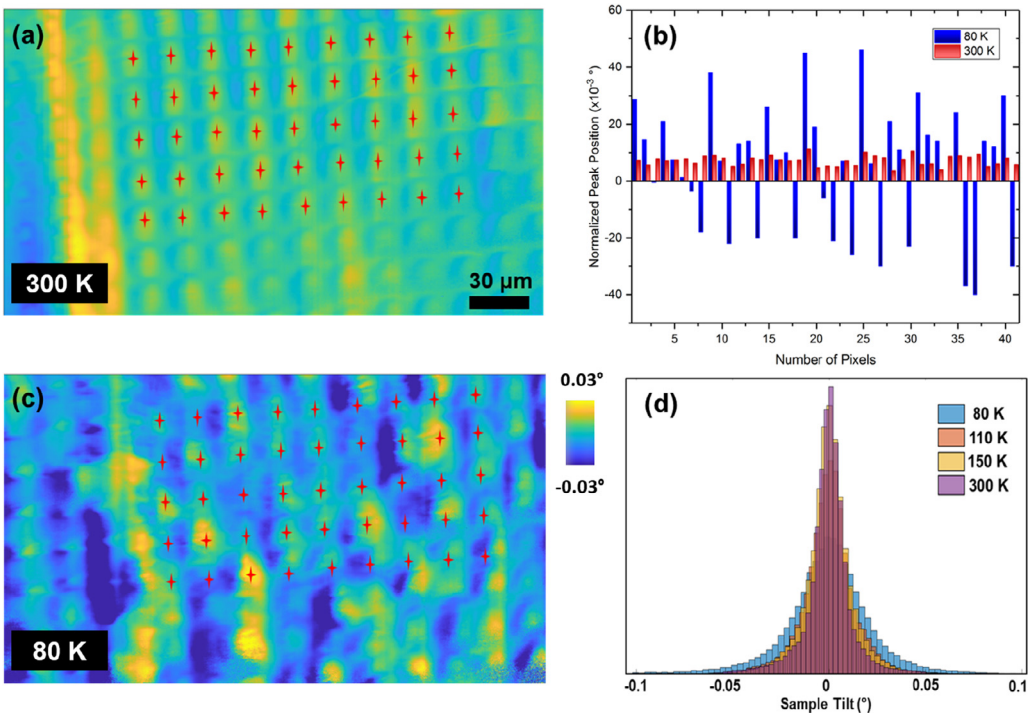

Fig. 4. Individual pixel orientation analysis. Reconstructed orientation peak position maps at (a) 300 K and (c) at 80 K. (b) Histogram of the peak position values at the red marks on selected pixels of the maps (a) and (c). (d) Total orientation distribution of the sum of all pixels at different temperatures. (For interpretation of the references to colour in this figure legend, the reader is referred to the web version of this article.)

form at 150K gradually increase intensity as the temperature is decreased down to 80K. Similar behaviour is observed for R5 as well. Note that the measured strain in the 333 Bragg reflection remains in the elastic regime (i.e. below the yield strength of MCT), in accordance with the literature [11,23,24]. The overall strain levels of Z2 are less than the strain measured at Z1 (not shown) by $\approx$ 40 %. This observation is in agreement with a recent study that shows the stress variations from the border of the detector to interior parts [25].

To see the lattice distortions, we carried out rocking curve scans of the same regions at same temperatures. Fig. 5(i) shows the FWHM values extracted from these rocking curve scans in Z2 at 5 different temperatures. A careful analysis of the rocking curve FWHM values marks a difference between variant 13 and 9. At room temperature the FWHM values of R1 and R2 are below 7×10^{-3} ° whereas R4 and R5 have higher FWHM values. The FWHM value of R3 lies in between these regions. Upon cooling down, structural modification occurs in such a way that the lattice distortions result in a fluctuation reflected on the FWHM values (i.e. 150 K). Further cooling restores the lattice distortion difference of R1 and R2 over R4 and R5.

3.2.3. FWHM Analysis on detector variants

Fig. 6 shows the FWHM of the orientation of variant 10 and variant 6 in Z3 (see Fig. 2(b)) at 300 K. We probed the entire length of the two variants in Z3 by scanning the sensor over 11 steps. This way we were able to cover about 3 mm distance on the sensor with 240 nm spatial resolution. Unlike the analyses done on Z2, these FWHM values were extracted from the room temperature measurements after a full temperature cycle comprising cooling down to 80 K and heating back to room temperature. At a first glance to Fig. 6, variant 10 shows less lattice distortion compared to variant 6 manifested by $\approx$ 2.5-3$\times$ 10^{-3} ° difference in FWHM.

Apart from the difference in FWHM values of the two variants, Fig. 6 also reveals an interesting picture of the nature of the variants. There is a well-defined trend of FWHM as a function of position within a given variant, where FWHM reaches a local minimum around the mid point of each variant. Furthermore, FWHM values increase towards the borders of the variants. This trend is valid for both variant 10 and variant 6, of course with different offsets due to the intrinsic differences of each variant. In this regard, we can infer that the connection points of different variants have increased strain and lattice distortion, whereas the distortion is minimum towards the interior of the variants. Note that this result is in accordance with the macroscopic strain state of the whole detector, where the strain values are higher towards the borders of the detector compared to the interior [25]. This may indicate that the P-N junctions result more homogeneous strain fields in the interior of the variants regardless of their geometry (i.e. different variants).

3.2.4. Temperature cycle and reversibility on Z3

Fig. 7 shows the orientation maps of a full cooling cycle down to 80 K of the middle part of the region Z3. At room temperature (Fig. 7(a)), the orientation map shows similar angular spread to what was observed in Z2, with slight changes due to the nature of different variants. This indicates that the sensor has good structural homogeneity. Upon cooling (i.e. the left column of Fig. 7) we observe a similar change to the other zones (Z1 and Z2). The overall angular spread increases while some compression and tension regions in coupled forms (high and low θ manifested by red and blue color) appear in the size of $\approx$ 4 sensor pixels. We shall address these features as *doublets* throughout the rest of the manuscript. These doublets start appearing even at the temperatures between 290 and 200 K (not shown), and they increase in number upon further cooling down. The number density of these doublets reach up to 10^3 cm^{-2} at 80 K, similar to what was observed in Z1 and Z2.

During this scan, we probed different regions in Z3 at each temperature decrements and increments, and returned to the mid point of Z3. This approach was chosen to scan a larger area of the

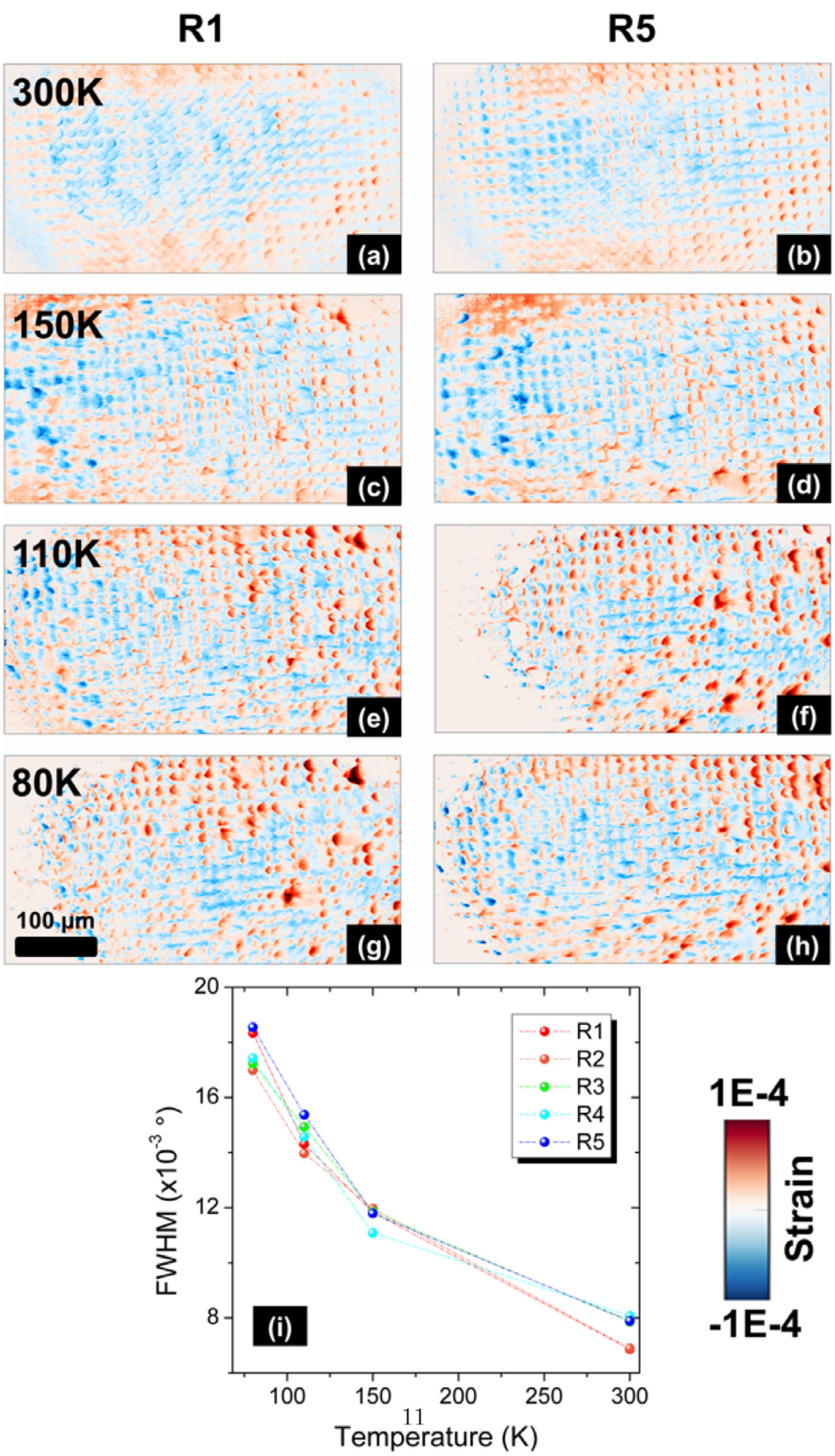

Fig. 5. (a-h) Axial strain maps of the selected two regions from V9 and V13 in the area Z2 as shown in Fig. 2(b) at different temperatures. R1 and R2 are situated in variant 13 and R4 and R5 in variant 9. R3 is located at the intersection of these two variants. (i) The rocking curve FWHM evolution as a function of temperature of the five region in Z2 area.

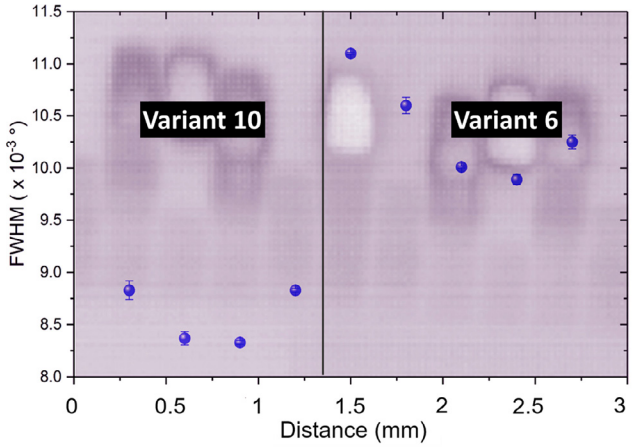

Fig. 6. FWHM values extracted from sample tilt scans of variant 10 and variant 6. The electrical responsivity map is superimposed on the graph to help visualize the spatial positions of each measurement point along the length at 300 K.

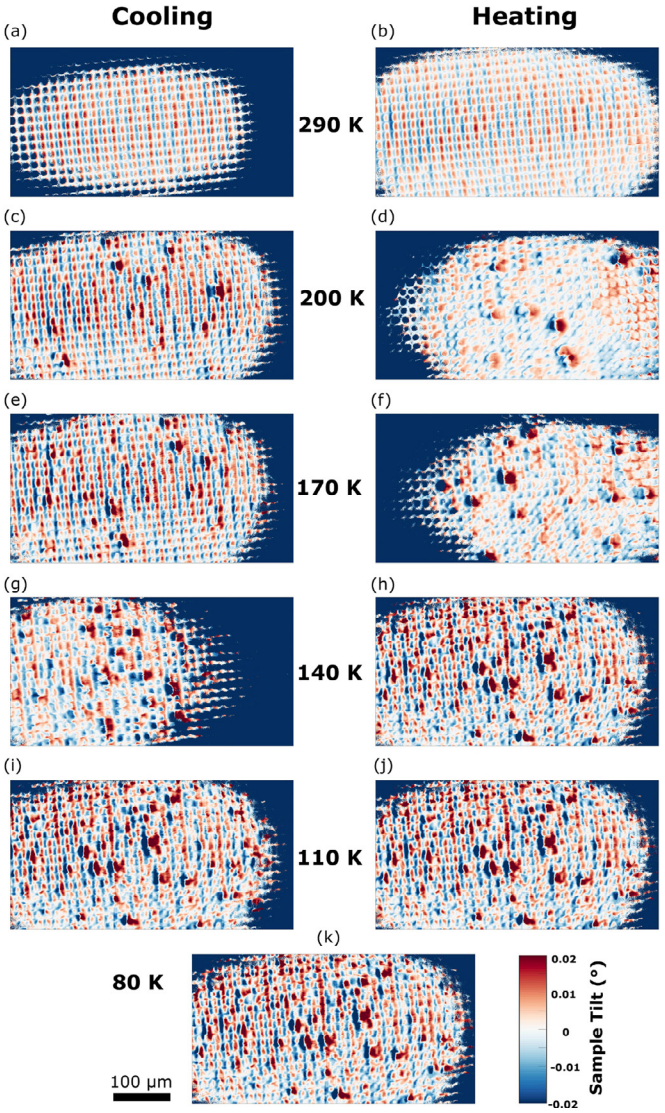

Fig. 7. Orientation maps of the mid part of Z3 during the temperature cycle, cooling down to 80 K and heating back up to room temperature.

sensor in a temperature cycle, while not overexposing the same zone by the X-rays. The results shown in Fig. 7 show almost the same zone within the field of view. Note that slight spatial shifts ($\approx$ 100 µm) occurred during the experiment due to the arm of the cryo-stream.

Upon heating from 80 K to 140 K, no drastic changes are observed in the angular spread. The overall FWHM decreases slowly as the temperature is increased, yet the coupled compression and tension regions remain the same. Starting from 140 to 170 K, a drastic change in the overall angular spread is observed. Nevertheless, the coupled regions still exist. Upon further heating, those doublets began to disappear, along with continuous decrease of the angular spread. Finally, the system is fully recovered once the ambient temperature is reached after one temperature cycle.

4. Discussion

A clear picture now emerges of how the IR sensor responds to the temperature changes. The global trend manifests a gradual increase in the measured strain upon cooling down to 80 K. Moreover, the measured strain is reversible over a full cooling/heating cycle from room temperature down to 80 K and the associated stress is below 30 MPa, remaining in the elastic region [24,26]. The coefficient of thermal expansion (CTE) difference between the ROIC and the MCT adds up to the contraction of MCT yet the measured strain still remains below the elastic limit. This observation is valid over the entire volume that was measured, showing the homogeneity of the sensor across different variants (Fig. 5). Nevertheless, slight differences in the FWHM values of the rocking curves were observed from one variant to the other, which indicates the effect of differences in mechanical contacts on the MCT strain state. Note that the FWHM increase (i.e. rocking curve peak broadening) upon reducing the temperature is attributed to the elastic lattice bending since the system fully recovered its initial FWHM after the completion of one thermal cycle (see the Supplementary Material).

Although the structural homogeneity is preserved during the thermal cycles, there are coupled compression and tension zones manifesting higher intensity on the reconstructed maps (higher misorientation and/or strain values) than the rest of the IR sensor that spans 2 to 4 IR pixels. The formation of these *doublets* is observed to be random upon cooling down. These features may emerge even at 200 K and increase in number as the temperature is further reduced. Moreover, there is no evident orientation relationship between these doublets and they are also reversible, meaning that they vanish upon heating up to room temperature.

In order to understand the formation of these doublets on the MCT pixels, one must consider the entire sensor. It is known that the CTE between the ROIC and MCT adds up to the measured strain, yet this is a rather homogeneous increase in the strain, unlike the *doublets*. One can speculate these doublets appear due to different mechanical contacts between the ROIC and the MCT, yet all studied variants show the doublets regardless. So what could be the reason for the emergence of the doublets? The answer may lie in the In bumps that connect the MCT to the ROIC within the epoxy matrix. It is known that In bumps with tetragonal crystal structure are highly anisotropic in their thermomechanical behavior [27–29]. Lebaudy et al. showed that the thermomechanical response of IR detector can yield notable variations due to random crystallographic orientations of the In bumps [30].

To study the effect of the orientations of In bumps on the strain on the MCT, we calculated the relative displacement on the MCT from the rocking curves, and compared it with the finite element modelling (FEM) calculations. Fig. 8 shows a comparison of the relative displacement of the MCT layer at 80 K between experimental and FEM results. The details of the parameters of the FEM analysis are given elsewhere [30]. The experimental relative displacement

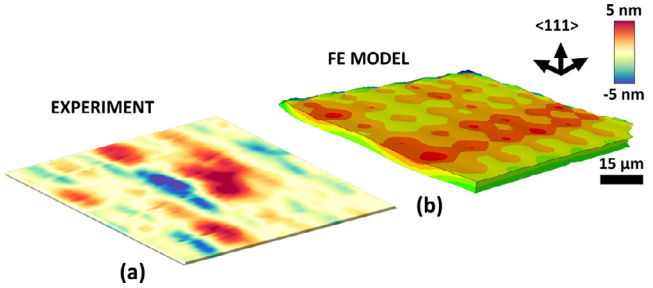

Fig. 8. Relative displacement comparison between the DFXM experiment and finite element modelling.

of the MCT was calculated using the normalized rocking curves by the following relation:

$$\Delta z = \tan(\Delta\theta) \times 7.5\mu\mathrm{m} \quad (1)$$

where $\Delta\theta$ is the angular deviation from the center of mass of the rocking curve and 7.5 µm is the half distance of a given IR pixel on the detector. Note that even though the average experimental displacement within the field of view is about ± 5 nm, locally the displacement values reach more than 33 nm around the doublets.

In Fig. 8(b), the regions with high displacement corresponds to the *most unfavorable* crystallographic orientation of tetragonal single crystal In bumps at 80 K [27]. It was reported that In bumps could be more in compression at 100 K depending on the In crystallographic orientation [25]. Numerical results showing the effect of orientation on the MCT strain state is shown in Supplementary Fig. 3. Even though our temperature cycle shows that these doublets disappear upon heating back to room temperature, one must conduct multiple temperature cycles to determine the reappearances of these doublets, should they form in the same zones. We speculate that these zones could lead to eventual cracks at the MCT/ROIC interface, resulting in dead pixels that degrade the performance of the IR sensor.

5. Conclusions

The present study investigated the nanoscale structural evolution over a large population of photodiodes down to operating temperatures (80 K). The strain and orientation states of MCT pixels were studied comprehensively at various length scales using DFXM. Our results show an increase in the axial strain upon cooling. The measured stress was below 30 MPa, thus in the elastic regime, and completely reversible through a full temperature cycle. We showed, for the first time, the strain evolution of individual pixels with quantitative statistical information over a 5 mm distance within an operable IR sensor. Moreover, this work presents the first ever successful proof-of-concept study for DFXM investigations using cryogenic conditions. The post-DFXM electrical characterization showed that the IR sensor was still operable. We complemented our DFXM studies with FEM analyses to assess the nature of the tension-compression *doublets* appearing below 200 K. We argue that the anisotropic coefficient of thermal expansion of In bumps results in the formation of these doublets due to random crystallographic orientations of the In bumps beneath MCT layer. We are aware that all our experimental observations of the In bump - MCT interactions are indirect, even though supported by FEM analyses. The experimental evidence of correlation between In bumps' orientation on the strain state of the MCT could potentially be observed by DFXM by probing different Bragg peaks of In and MCT. Our work in this direction is in progress. These results illustrate the capabilities of DFXM in IR detector studies and open up new avenues for further experiments in which several thermal cycles can be applied along with an electrical field to study operando. Our results are highly anticipated to improve the IR sensor quality and functionality at real operation conditions, which will allow for new insights on the strain state of the HgCdTe layer of IR sensors and validate structural models.

Declaration of Competing Interest

The authors declare that they have no known competing financial interests or personal relationships that could have appeared to influence the work reported in this paper.

Acknowledgement

We thank the ESRF for provision of beamtime at ID01.C.Y. acknowledges P.K. Cook for the meticulous proofreading.

Supplementary material

Supplementary material associated with this article can be found, in the online version, at doi:10.1016/j.actamat.2021.117290.

References

[1] O. Gravrand, J. Rothman, C. Cervera, N. Baier, C. Lobre, J. Zanatta, O. Boulade, V. Moreau, B. Fieque, Hgcdte detectors for space and science imaging: general issues and latest achievements, J. Electron. Mater. 45 (9) (2016) 4532–4541.
[2] D. Lee, M. Carmody, E. Piquette, P. Dreiske, A. Chen, A. Yulius, D. Edwall, S. Bhargava, M. Zandian, W. Tennant, High-operating temperature hgcdte: a vision for the near future, J. Electron. Mater. 45 (9) (2016) 4587–4595.
[3] O. Gravrand, G. Destefanis, S. Bisotto, N. Baier, J. Rothman, L. Mollard, D. Brellier, L. Rubaldo, A. Kerlain, V. Destefanis, et al., Issues in hgcdte research and expected progress in infrared detector fabrication, J. Electron. Mater. 42 (11) (2013) 3349–3358.
[4] P. Ballet, A. Jonchère, B. Amstatt, X. Baudry, B. Polge, D. Brellier, P. Gergaud, Mismatch and thermal strain analysis in mbe-grown hgcdte/cdznte, J Cryst Growth 371 (2013) 130–133.
[5] A. Tuaz, P. Ballet, X. Biquard, F. Rieutord, Micro-diffraction investigation of localized strain in mesa-etched hgcdte photodiodes, J. Electron. Mater. 46 (9) (2017) 5442–5447.
[6] X. Biquard, P. Ballet, A. Tuaz, P. Jouneau, F. Rieutord, Submicronic laue diffraction to determine in-depth strain in very closely matched complex hgcdte/cdznte heterostructures with a 10- 5 resolution, J Synchrotron Radiat 28 (1) (2021).
[7] M. Zécri, P. Maillart, E. Sanson, G. Decaens, X. Lefoul, L. Baud, Advanced roics design for cooled ir detectors, in: Infrared Technology and Applications XXXIV, 6940, International Society for Optics and Photonics, 2008, p. 69402X.
[8] M. Vuillermet, P. Tribolet, Operating temperature: a challenge for cooled ir technologies, in: Infrared Technology and Applications XXXVI, 7660, International Society for Optics and Photonics, 2010, p. 76602U.
[9] M. Kinch, R. Strong, C. Schaake, 1/F noise in hgcdte focal-plane arrays, J. Electron. Mater. 42 (11) (2013) 3243–3251.
[10] M.S. Cabrera, C.W. McMurtry, M.L. Dorn, W.J. Forrest, J.L. Pipher, D. Lee, Development of 13-cutoff hgcdte detector arrays for astronomy, J. Astron. Telesc. Instrum. Syst. 5 (3) (2019) 036005.
[11] P. Ballet, X. Baudry, B. Polge, D. Brellier, J. Merlin, P. Gergaud, Strain determination in quasi-lattice-matched lwir hgcdte/cdznte layers, J. Electron. Mater. 42 (11) (2013) 3133–3137.
[12] P. Gergaud, A. Jonchere, B. Amstatt, X. Baudry, D. Brellier, P. Ballet, X-Ray diffraction investigation of thermoelastic properties of hgcdte/cdznte structures, J. Electron. Mater. 41 (10) (2012) 2694–2699.
[13] H. Simons, A. King, W. Ludwig, C. Detlefs, W. Pantleon, S. Schmidt, F. Stöhr, I. Snigireva, A. Snigirev, H.F. Poulsen, Dark-field x-ray microscopy for multiscale structural characterization, Nat Commun 6 (1) (2015) 6098.
[14] K.T. Murray, A.F. Pedersen, I. Mohacsi, C. Detlefs, A.J. Morgan, M. Prasciolu, C. Yildirim, H. Simons, A.C. Jakobsen, H.N. Chapman, H.F. Poulsen, S. Bajt, Multilayer laue lenses at high x-ray energies: performance and applications, Opt. Express 27 (5) (2019) 7120–7138, doi:10.1364/OE.27.007120.
[15] N. Mavrikakis, C. Detlefs, P. Cook, M. Kutsal, A. Campos, M. Gauvin, P. Calvillo, W. Saikaly, R. Hubert, H. Poulsen, A. Vaugeois, H. Zapolsky, D. Mangelinck, M. Dumont, C. Yildirim, A multi-scale study of the interaction of sn solutes with dislocations during static recovery in α- fe, Acta Mater 174 (2019) 92–104, doi:10.1016/j.actamat.2019.05.021.
[16] J. Hilhorst, F. Marschall, T.N. Tran Thi, A. Last, T.U. Schülli, Full-field X-ray diffraction microscopy using polymeric compound refractive lenses, J Appl Crystallogr 47 (6) (2014) 1882–1888, doi:10.1107/S1600576714021256.
[17] E. Mottin, P. Pantigny, R. Boch, Improved architecture of irfpa readout circuits, in: Infrared Technology and Applications XXIII, 3061, International Society for Optics and Photonics, 1997, pp. 117–126.
[18] G. Destefanis, Hgcdte infrared diode arrays, Semicond Sci Technol 6 (12C) (1991) C88.

[19] S.J. Leake, G.A. Chahine, H. Djazouli, T. Zhou, C. Richter, J. Hilhorst, L. Petit, M.-I. Richard, C. Morawe, R. Barrett, L. Zhang, R.A. Homs-Regojo, V. Favre-Nicolin, P. Boesecke, T.U. Schülli, The nanodiffraction beamline ID01/ESRF: a microscope for imaging strain and structure, J Synchrotron Radiat 26 (2) (2019) 571–584, doi:10.1107/S160057751900078X.
[20] G.D. Jenkins, C.P. Morath, V.M. Cowan, Empirical study of the disparity in radiation tolerance of the minority-carrier lifetime between ii–vi and iii–v mwir detector technologies for space applications, J. Electron. Mater. 46 (9) (2017) 5405–5410.
[21] E.H. Steenbergen, C.P. Morath, D. Maestas, G.D. Jenkins, J.V. Logan, Comparing ii-vi and iii-v infrared detectors for space applications, in: Infrared Technology and Applications XLV, 11002, International Society for Optics and Photonics, 2019, p. 110021B.
[22] S.R. Ahl, Elements of a method for multiscale characterization of recrystallization in deformed metals, 2018,.
[23] K. Guergouri, R. Triboulet, A. Tromson-Carli, Y. Marfaing, Solution hardening and dislocation density reduction in cdte crystals by zn addition, J Cryst Growth 86 (1–4) (1988) 61–65.
[24] R. Irwan, H. Huang, H. Zheng, H. Wu, Mechanical properties and material removal characteristics of soft-brittle hgcdte single crystals, Materials Science and Engineering: A 559 (2013) 480–485.
[25] A.-L. Lebaudy, R. Pesci, M. Fendler, X-Ray diffraction residual stress measurement at room temperature and 77 k in a microelectronic multi-layered single-crystal structure used for infrared detection, J. Electron. Mater. 47 (11) (2018) 6641–6648.
[26] P. Ballet, X. Baudry, B. Polge, D. Brellier, J. Merlin, P. Gergaud, Strain determination in quasi-lattice-matched lwir hgcdte/cdznte layers, J. Electron. Mater. 42 (11) (2013) 3133–3137.
[27] D. Winder, C.S. Smith, Single-crystal elastic constants of indium, J. Phys. Chem. Solids 4 (1–2) (1958) 128–134.
[28] J. Collins, J. Cowan, G. White, Thermal expansion at low temperatures of anisotropic metals: indium, Cryo 7 (1–4) (1967) 219–224.
[29] J. Smith, V. Schneider, Anisotropic thermal expansion of indium, Journal of the Less Common Metals 7 (1) (1964) 17–22.
[30] A.-L. Lebaudy, R. Pesci, B. Piotrowski, Multilayer cdhgte-based infrared detector: 2d/3d microtomography, synchrotron emission and finite element modelling with stress distribution at room temperature and 100 k, Materialia 9 (2020) 100511.